The Journal of Chemical Physics

RESEARCH ARTICLE | APRIL 03 2026

Molecular contributions to the thermal neutron cross sections of O_2, N_2, and air

Margherita Simoni ; Felix Fernandez-Alonso ; Tommaso Giovannini ; Matthew Krzystyniak ; Jose Ignacio Marquez Damian ; Anna Marsicano ; Marco Martellucci; Triestino Minniti ; Roberto Senesi ; Matteo Sorbara ; Giovanni Romanelli

J. Chem. Phys. 164, 134109 (2026)
https://doi.org/10.1063/5.0324136

AIP Publishing

The Journal
of Chemical Physics

ARTICLE

pubs.aip.org/aip/jcp

Molecular contributions to the thermal neutron cross sections of O_2, N_2, and air

Cite as: J. Chem. Phys. **164**, 134109 (2026); doi: 10.1063/5.0324136
Submitted: 22 January 2026 • Accepted: 18 March 2026 •
Published Online: 3 April 2026

View Online Export Citation CrossMark

Margherita Simoni,[1] **Felix Fernandez-Alonso**,[2,3,4] **Tommaso Giovannini**,[1] **Matthew Krzystyniak**,[5] **Jose Ignacio Marquez Damian**,[6] **Anna Marsicano**,[5] **Marco Martellucci**,[1] **Triestino Minniti**,[1] **Roberto Senesi**,[1,7] **Matteo Sorbara**,[1] **and Giovanni Romanelli**[1,5,a)]

AFFILIATIONS

[1] Physics Department, Università degli Studi di Roma Tor Vergata, via della Ricerca Scientifica 1, 00133 Roma, Italy
[2] Centro de Física de Materiales (CFM-MPC), CSIC-UPV/EHU, Paseo de Manuel Lardizabal 5, Donostia 20018, Gipuzkoa, Spain
[3] Donostia International Physics Center (DIPC), Paseo de Manuel Lardizabal 4, 20018 Donostia - San Sebastian, Spain
[4] IKERBASQUE, Basque Foundation for Science, Plaza Euskadi 5, 48009 Bilbao, Spain
[5] ISIS Neutron and Muon Source, Rutherford Appleton Laboratory, Chilton OX11 0QX, United Kingdom
[6] European Spallation Source, ESS ERIC, Partikelgatan 2, 224 84 Lund, Sweden
[7] Istituto di Struttura della Materia (ISM), Consiglio Nazionale delle Ricerche, Via del Fosso del Cavaliere, 100, Rome 00133, Italy

[a)] **Author to whom correspondence should be addressed:** giovanni.romanelli@uniroma2.it. **Permanent address:** University of Rome Tor Vergata, 00133, Rome, Italy. **Telephone:** +390672594441

ABSTRACT

We provide an updated scattering library for the simulation of thermal neutron transport in air, including the effects of rotational and vibrational modes in N_2 and O_2 and neutron magnetic scattering in O_2, showing their significance compared to smaller effects related to water humidity. The modeling is based on the Young–Koppel treatment of thermal neutron scattering from diatomic molecules, as well as *ab initio* simulations of the electronic density of O_2. The theoretical predictions are benchmarked against experimental measurements of the total scattering cross section of air under monitored thermophysical conditions, in the neutron energy range between 0.6 meV and 10 keV. The updated scattering library is used to calculate excess neutron scattering in air, compared to traditional approaches, where only nuclear scattering from gases of free nuclei is implemented in Monte Carlo transport codes.

I. INTRODUCTION

An accurate determination of the energy-dependent total cross section of neutrons by air is beneficial for a number of experimental activities, including the determination of the lifetime of the neutron,[1] the optimized design of neutron instruments and beamlines,[2] and the accurate assessment of argon activation in medical facilities. Detailed experimental measurements of N_2 and O_2 were already presented in 1949 in a comprehensive article by Melkonian.[3] However, some sources of experimental uncertainties at early-days neutron sources (see Sec. 3 of Ref. 3) are no longer an issue at modern facilities, while other sources of systematic uncertainties, such as the determination of the thickness of non-solid samples, have remained a relevant problem (see Sec. 5 of Ref. 3 as well as the more recent Refs. 4 and 5). In this framework, some experimental cross sections needed revisions, as for the value of the capture cross section of nitrogen—reported in Ref. 3 more than 12% larger than the one routinely accepted at present[6]—or in the case of para-H_2—recently revisited in Ref. 7. From the theoretical point of view, the modeling of neutron-nucleus scattering by N_2 and O_2 diatomic molecules, mainly based on the Young and Koppel (YK) model,[8] requires taking into account transitions between tens of molecular rotational states, which entails a computational effort ably avoided by insightful approximations in the past.[9] This is due to the small rotational energy constants of these molecules as compared with the thermal energy contribution k_BT at room temperature, with

T being the thermodynamic temperature and k_B being the Boltzmann constant—a problem not encountered in the more famous case of molecular hydrogen.[7] In the case of O_2, the additional inclusion of neutron–electron magnetic scattering suffered from arbitrary assumptions on the shape of the molecular orbitals hosting the two unpaired electrons, which give the molecule its paramagnetic properties (see Sec. 6 of Ref. 9). This possibly led to some strange results, such as the nonphysical energy dependence of the magnetic cross section reported in Ref. 10. In this sense, it is interesting to notice how magnetic neutron scattering has evolved as a technique for materials characterization mainly for solids,[11,12] while no recent investigation on simple diatomic molecules such as O_2 has been provided, to the best of our knowledge.

Notwithstanding such difficulties, simple diatomic molecules provided an early and exciting testbed to develop the theory of both nuclear and magnetic neutron scattering, as shown by the above-mentioned work on pure samples. Meanwhile, air—as a ubiquitous composite gas—did not attract a similar interest. Air is composed of several gases, among which N_2 and O_2 are the most abundant ones. However, the molecule attracting most attention has been H_2O as vapor. It is well known that H has the largest neutron scattering cross section among the elements of the Periodic Table, and it has been argued that small amounts of water vapor could significantly change the scattering and attenuation properties of air. Recently, Barker and Mildner[2] reported experimental results on the macroscopic neutron cross section of air using the Sachs–Teller corrected free-gas model,[13] where the nuclear mass is replaced with an effective parameter, which approximately includes the effect of molecular rotations. However, experimental results above 5 Å (energies lower than 3.3 meV) were found to be about 10%–15% higher than the prediction from this simplified model, and this discrepancy was qualitatively attributed to a possibly higher water content in the sample considered.

Here, we provide a new determination of the air neutron cross section under controlled thermophysical conditions, in an extended energy range between 0.6 meV and 10 keV. Moreover, we performed updated calculations of the nuclear scattering cross section of N_2 and O_2, including all transition terms between molecular rotational states, and we calculated the magnetic neutron–electron scattering based on state-of-the-art computer simulations. Comparisons based on varying levels of humidity and the inclusion/exclusion of molecular contributions are discussed to show that the latter are of greater importance than the former. Finally, we provide a worked example discussing the radiation protection implications of including an accurate cross section of air in Monte Carlo models.

II. MATERIALS AND METHODS

A. Cross section modeling

The neutron double differential scattering cross section can be expressed, through the application of the Fermi golden rule, as

$$\frac{d^2\sigma_s}{d\Omega dE'} = \left(\frac{m_n}{2\pi\hbar^2}\right)^2 \sum_i P_i \sum_f \frac{k'}{k} \times \left|\langle i|V(\vec{Q})|f\rangle\right|^2 \times \delta\left(\Delta E + E_i - E_f\right), \tag{1}$$

where $d\Omega$ is the solid angle, at which a neutron of final energy between E' and $E' + dE'$ is scattered, $\Delta E = E - E'$ and $\mathbf{Q} = \mathbf{k} - \mathbf{k}'$ are the neutron energy and wave-vector transfer, respectively, E_i and E_f are the initial and final energies of the scattering system, respectively, m_n is the neutron mass, and $\hbar$ is the Dirac constant. The equation requires averaging over all initial states $|i\rangle$, weighted by their relative probability P_i, and summing over their final states $|f\rangle$. The interaction potential can be expressed as the sum of a nuclear and a magnetic contribution,

$$V(\mathbf{Q}) = V_N(\mathbf{Q}) + V_M(\mathbf{Q}) = \int e^{i\mathbf{Q}\cdot\mathbf{r}}[V_N(\mathbf{r}) + V_M(\mathbf{r})]d\mathbf{r}, \tag{2}$$

by assuming that incident and scattered neutrons travel as plane waves, in the case of short-range scattering potentials. Since the cross section depends on the square of the matrix element of $V(\mathbf{Q})$, it can be separated into three contributions: a purely nuclear term, which in the case of O_2, can be evaluated using the YK model described before, a purely magnetic term, and a nuclear-magnetic interference term. The latter averages out if neutrons are unpolarized, and therefore, it will not be considered.

Unless explicitly stated, all figures in this article report total cross sections, $\sigma_t(E) = \sigma_s(E) + \sigma_a(E)$, that is, the sum of the scattering cross section,

$$\sigma_s(E) = \int d\Omega \int dE' \frac{d^2\sigma_s}{d\Omega dE'}, \tag{3}$$

and the absorption cross section, $\sigma_a(E) = \sigma_a(E_0)\sqrt{E_0/E}$, with the reference values of absorption calculated at $E_0 = 25.3$ meV obtained from Ref. 6.

1. Nuclear scattering

The interaction potential in the case of nuclear scattering by a homonuclear molecule with nuclei at positions $\vec{R}_1$ and $\vec{R}_2$ can be expressed through the simplified Fermi potential as

$$V_N(\mathbf{r}) = \frac{2\pi\hbar^2}{m_N}\hat{b}_N(\delta(\mathbf{r} - \mathbf{R}_1) + \delta(\mathbf{r} - \mathbf{R}_2)), \tag{4}$$

where $\hat{b}_N$ is the nuclear scattering length operator. The double differential cross section defined by Eq. (1) can be calculated by assuming that the wavefunctions $|i\rangle$ and $|f\rangle$, describing the system before and after the scattering event, can be expressed as the product of translational, rotational, and vibrational terms, assuming that these motions are not coupled. Moreover, translational modes can be approximated through a free motion of the center of mass, as in the kinetic theory of gases. Furthermore, vibrational modes can be taken into account by assuming that the initial state is, for any practical case, in the vibrational ground state, and transitions to higher states are related to a harmonic restoring force between the two nuclei. Finally, rotational contributions, related to the less trivial features of the thermal scattering cross section, are discussed in more detail below.

Both oxygen and nitrogen nuclei obey the Bose–Einstein statistics, having an integer nuclear spin i, with $i_O = 0$ in the case of oxygen and $i_N = 1$ in the case of nitrogen. When two such nuclei are combined in a homonuclear diatomic molecule, the nuclear spins combine to create a state of total nuclear spin I, with $I_{O_2} = 0$ and $I_{N_2} = 0, 1, 2$. Following the Bose–Einstein statistics, if the electronic wavefunction is symmetric, the state with even values of $I = 0, 2$ can

TABLE I. Total symmetry of the molecular wavefunction, as the product of the symmetry of (nuclear spin) × (rotational) × (electronic) wavefunctions, respectively. Experimental neutron scattering lengths $b^{(\pm)}$ and molecular radii r_e are also reported.

Molecule	Total sym.	I	J	Electronic ground state	$b^{(+)}$ (fm)	$b^{(-)}$ (fm)	r_e (Å)
N_2	S = S × S × S	2 (ortho)	0, 2, . . .	$1\Sigma_g^+$	1.08	0.65	1.097 68
	S = A × A × S	1 (para)	1, 3, . . .				
	S = S × S × S	0 (ortho)	0, 2, . . .				
O_2	S = S × A × A	0 (ortho)	1, 3, . . .	$3\Sigma_g^-$	0.5805	0.5805	1.207 52

only exist in even rotational states, $J = 0, 2, \ldots$. Conversely, states with an odd value of $I = 1$ can only exist in odd rotational states. In the case of O_2, the two unpaired electrons in the ground state result in an antisymmetric electronic wavefunction; consequently, the rotational wavefunction must be antisymmetric to ensure that the overall molecular wavefunction is symmetric.[14] The symmetry requirements on the two molecules are summarized in Table I. Their experimental neutron scattering lengths $b^{(\pm)}$ and molecular radii r_e are also reported in this table. It is worth reminding that such symmetries are constructed by imposing that the resulting spin state with the highest value needs to be symmetric, and the following states with decreasing values need to alternate between symmetric (S) and antisymmetric (A). The states that are symmetric with respect to the nuclear-spin wavefunction are referred to as *ortho* modifications, and the other (antisymmetric) states are referred to as *para* modifications.

From this discussion, it follows that neutron scattering processes involving a nuclear spin flip ($|\Delta I| = |I' - I| = 1$) are associated with the transitions of the angular momentum from an initial state J to a final state J' such that $\Delta J = J' - J$ equals an odd integer, while scattering events with no nuclear spin flip ($\Delta I = 0$) are associated with transitions where ΔJ equals an even integer. As nuclear spin flips need to be compensated by neutron spin flips, one can expect that the former interactions involve the incoherent scattering parameter, while the latter interactions involve the coherent scattering parameter. In particular, one can write the scattering length operator as[15]

$$\hat{\mathbf{b}}_N = C_1 + \frac{1}{2} C_2 \left(\hat{\mathbf{s}}_{\mathbf{n}} \cdot \hat{\mathbf{i}} \right), \tag{5}$$

where $\hat{\mathbf{s}}_{\mathbf{n}}$ is the neutron spin operator, $\hat{\mathbf{i}}$ is the nuclear spin operator, and the parameters C_1 and C_2 are related to the experimental neutron scattering lengths $b^{(\pm)}$ from the neutron–nucleus compound state $i \pm \frac{1}{2}$,

$$C_1 = \frac{i}{2i+1} \left[(i+1) b^{(+)} + i b^{(-)} \right] \tag{6}$$

and

$$C_2 = \frac{2}{2i+1} \left[b^{(+)} - b^{(-)} \right]. \tag{7}$$

The scattering from the homonuclear diatomic molecule is then associated with two cases: $\Delta I = 0$ and ΔJ even (case e) and $\Delta I = 0$ and ΔJ odd (case o). By applying the scattering length operator to these two cases, one finds that the associated cross section parameters are

$$\sigma_e^{(I)} = 4C_1^2 + \frac{1}{4} C_2^2 I(I+1) \tag{8}$$

and

$$\sigma_o^{(I)} = \frac{1}{4} C_2^2 [4i(i+1) - I(I+1)]. \tag{9}$$

The above discussion brings to the final form of the YK double-differential scattering cross section,[8]

$$\frac{d^2\sigma_s(E,I)}{dE'd\Omega} = \frac{k'}{k} \sum_J P_J \sum_{J'} (2J'+1) \Big[\sigma_e^{(I)} f_{J,J'}(Q,\omega) (\text{ if } \Delta J = even) + \sigma_o^{(I)} f_{J,J'}(Q,\omega) (\text{ if } \Delta J = odd) \Big], \tag{10}$$

with the function $f_{J,J'}(Q,\omega)$ defined as

$$f_{J,J'}(Q,\Delta E) = \frac{\exp\left(-\frac{(\Delta E_J - E_R - \Delta E)^2}{2k_B T E_R} \right)}{\sqrt{2\pi k_B T E_R}} \sum_{l=|J-J'|}^{J+J'} (2l+1) \times \begin{pmatrix} J' & J & l \\ 0 & 0 & 0 \end{pmatrix}^2 j_l^2 \left(\frac{Qr_e}{2} \right), \tag{11}$$

which includes a sum over all allowed values of the angular momentum l, according to the sum rules of quantum angular momenta, which is included and weighted by the Wigner $3-j$ coefficients. It is important to note that this equation strictly models only the scattering cross section for neutron energies lower than the molecular vibrational energy, that is, 196 meV for O_2 and 292 meV for N_2. However, as discussed below, this energy range is the one manifesting, in the experimental cross section, the most important differences compared to standard models based on the free-nuclear-gas approximation. Moreover, values of P_J can be obtained from a Boltzmann partition function, considering that the rotational energy associated with each initial state, namely $E_J = BJ(J+1)$ with $B = \hbar^2/(Mr_e^2)$ and the molecular radius $r_e = |\vec{R}_1 - \vec{R}_2|/2$. The recoil energy of the molecule has also been defined as $E_R = (\hbar Q)^2/(4M)$. It is worth noting that the YK formalism requires the use of the molecular recoil energy, which is responsible for the shift of inelastic neutron scattering peaks of light diatomic molecules,[16] rather than the nuclear recoil energy, which would be employed within the impulse approximation at higher neutron energies.

2. Magnetic scattering

The intrinsic magnetic dipole moment of neutrons is responsible for their coupling with the microscopic paramagnetic field of molecular oxygen. This potential can be expressed as the coupling of the neutron dipole moment $\boldsymbol{\mu}_n$ and the local magnetic flux density $\mathbf{B}(\mathbf{r})$ as

$$V_M(\mathbf{r}) = -\boldsymbol{\mu}_n \cdot \mathbf{B}(\mathbf{r}), \tag{12}$$

where the local magnetic flux density is related to the transversal component of the microscopic magnetization due to the unpaired electron spin in the molecular orbital $3\Sigma_g^-$, with total spin $S = 1$, and the neutron dipole moment $\boldsymbol{\mu}_n = -2\gamma\mu_N \boldsymbol{s_n}$, with $\gamma = 1.913$ being the magnetic moment of neutrons expressed in nuclear magnetons μ_N. Calculating the matrix element of the magnetization can be an extremely demanding task; therefore, we make use of the dipole approximation. The approximation is based on the principle that magnetic neutron scattering can be expressed as a sum of multipole moments, as in Ref. 17. When $\mathbf{Q}$ is smaller than the reciprocal of the atomic radius, the dipole term dominates the magnetic scattering cross section, but in most cases, this approximation has proven to be satisfactory even for larger values of $\mathbf{Q}$.[12] Moreover, the matrix element of the magnetization can be approximated assuming that the electronic spin is not coupled to the angular electronic momentum. This assumption is justified by experimental results obtained by Van Vleck.[18] Therefore, one has

$$\mathbf{B}(\mathbf{Q}) = \mu_0 \mathbf{M}(\mathbf{Q}) = -2\mu_B\mu_0 f(\mathbf{Q})\mathbf{S}. \tag{13}$$

With these assumptions, and considering the magnetic scattering purely elastic, the magnetic differential scattering cross section is

$$\frac{d\sigma_s}{d\Omega} = \frac{2}{3}\left(\frac{\mu}{m_n}\right)^2 \gamma^2 r_0^2 S(S+1) e^{-2W(Q)} f^2(Q), \tag{14}$$

where μ is the reduced mass of the oxygen molecule–neutron system, $r_0 = \mu_0 e^2/(4\pi m_e c^2) = 2.818 \times 10^{-5}$ Å is the classical electron radius, S is the total electronic spin, and $W(Q)$ is the Debye–Waller factor. In the dipole approximation for a system dominated by electronic spin, it can be expressed as[12]

$$f(Q) = \int_0^\infty j_o(Qr) r^2 R^2(r) dr, \tag{15}$$

where $R(r)$ is the radial electronic wavefunction.

B. Radial spin density calculation

The term $r^2R^2(r)$ was calculated using both static and dynamic approaches. First, static calculations were performed at the Density Functional Theory (DFT) and post-Hartree–Fock (HF) coupled-cluster singles and doubles (CCSD) levels.[19] Second, *ab initio* Molecular Dynamics (MD) simulations at the DFT level were performed for the sake of comparison.

1. DFT and CCSD simulations

The geometry of O_2 in the gas phase was optimized at the B3LYP/aug-cc-pVTZ level of theory. The spin density was then calculated at the B3LYP[20,21]/aug-cc-pVTZ and post-HF CCSD/aug-cc-pVTZ levels. In particular, for CCSD/aug-cc-pVTZ calculations, spin densities were computed by performing orbital optimization. In both cases, GAUSSIAN CUBE files were generated and exploited for the following numerical analysis. All the calculations were performed using ORCA 5.0.[22]

2. Ab initio molecular dynamics simulations

The equilibrium structure of the isolated O_2 molecule was first optimized using the CASTEP code (Academic Release 22.11)[23] to ensure full consistency with the subsequent finite-temperature dynamics. The optimization was performed in a fixed cubic simulation cell of 10 Å side length under periodic boundary conditions. Electron–ion interactions were represented by a norm-conserving pseudopotential for oxygen, within the BLYP exchange–correlation functional, using the Koelling–Harmon scalar-relativistic treatment. The pseudopotential included a partial-core correction with a radius of 0.842 Å, and its transferability was confirmed by the absence of ghost states up to 40.6 eV. A plane wave cutoff of 1020 eV and a Γ-point sampling of the Brillouin zone were employed. Spin polarization corresponding to the triplet ground state (a net spin moment of 1 $\hbar$) was retained, and a Gaussian smearing of 0.1 eV was used to aid self-consistent convergence. Geometry optimization was carried out using the limited-memory BFGS algorithm with the stress tensor disabled and the cell dimensions fixed. Convergence was achieved when the maximum atomic force fell below 0.005 eV Å^{-1}, the total energy change was less than 10^{-6} eV per step, and atomic displacements were smaller than 5×10^{-4} Å.

Subsequent *ab initio* MD simulations were performed under identical electronic-structure conditions to preserve the continuity of the potential-energy surface. The dynamics employed the canonical (NVT) ensemble at 300 K, controlled via a Nosé–Hoover chain thermostat comprising five coupled thermostats with a characteristic ionic period of 0.001 ps. The integration time step was 0.001 ps, and the trajectory was propagated for 1300 steps, corresponding to a total simulation time of 1.3 ps. Wavefunctions and charge densities from the converged optimization were used as the initial electronic state through the `continuation` option, ensuring smooth energy conservation in the early stages of dynamics. Electronic minimization was conducted using ensemble DFT with one steepest-descent and four conjugate-gradient steps per self-consistent cycle, with a convergence threshold of 10^{-6} eV per atom. A Gaussian smearing of 0.1 eV was maintained, and a maximum of 100 SCF iterations was allowed per step. Both binary and formatted checkpoint files were written every five steps, enabling subsequent analysis.

To analyze electronic properties along the trajectory, atomic coordinates of O_2 were extracted from the MD trajectory file every 200 MD steps. For each snapshot, SinglePoint CASTEP calculations were performed to generate charge densities in the GAUSSIAN CUBE file format. The GAUSSIAN CUBE files were subsequently averaged over the entire set of 200 snapshots.

C. Air cross section modeling

The molecular gas models for O_2 and N_2 cross sections were finally combined to produce two models for air cross section: one representing dry air and the other incorporating the effects of humidity. In the dry-air model, the composition was taken to be 78.11% N_2, 20.95% O_2, and 0.94% argon. Each species was taken to consist solely of its most abundant isotope (^{14}N, ^{16}O, ^{40}Ar).

For simplicity, the nitrogen contribution was approximated using only the value corresponding to the total nuclear spin I = 1. In fact, the largest changes in cross section with nuclear spin occur in the low energy region. In particular, the scattering cross section of N_2 at 1 meV varies from 49.98 barn, for I = 0, to 51.18 barn, for I = 2. The value for I = 1 is 50.38 barn, which differs by only about 0.7% from the concentration-weighted value of 50.74 barn. The same relative composition was employed in the hydrated air model, rescaling it to add the water contribution. The mole percentage of H_2O molecules was estimated with the use of the empirical formula reported in Appendix A of Ref. 24, based on the measurements of relative humidity and temperature, acquired during the neutron transmission experiment and assuming a pressure of 1 atm. The H_2O contribution to the cross section was approximated using the CAB liquid water model by Marquez-Damian *et al.*[25–29] This is an approximation, considering that translational and rotational dynamics in water vapor and the liquid are expected to be qualitatively different. However, the corresponding changes to the macroscopic scattering cross section of air are expected to be negligible in the present case, also considering that water is a minor component of the gas.

D. Transmission measurements

Neutron transmission experiments were performed using the VESUVIO spectrometer at the ISIS Neutron and Muon Source.[30,31] The experiments were carried out by filling the instrument vacuum pipe and sample volume with environmental air, whose pressure, temperature, and relative humidity were constantly monitored during the measurement. This resulted in an effective cylindrical volume of 3.65 m length and 10 cm diameter filled with gas at ambient pressure, isolated from the environment during the neutron measurement. The experimental neutron transmission at 100 meV was 0.86. Considering the extended sample, the validity of the good-geometry approximation for the transmission measurement was tested through Monte Carlo simulations, described below (see Fig. 10). The number of neutrons scattered within its volume and the surrounding environment and detected by the transmission detector was compared to the number of detected transmitted neutrons, and their ratio was found negligible compared to the experimental relative error bar, which is related to the counting statistics.

The composition of dry air is fixed as 78.11% N_2, 20.95% O_2, and 0.94% argon. Direct measurement of humidity and temperature during the entire measurement provided values of a relative humidity (R.H.) of 56.5 ± 0.2 % and a temperature of 294.9 ± 0.2 K. The agreement between the experimental and theoretical results will be an *a posteriori* validation of this approximation. Measurements were performed using the time-of-flight (ToF) technique. Routinely, instruments in the ISIS Target Station 1 (TS1) can measure in the ToF region 0–20 ms, which on VESUVIO corresponds to a lower limit of 2.6 meV for the neutron energy. In this experiment, we used the possibility to extend the ToF range to 40 ms, as discussed in Ref. 32 obtained at ISIS TS1 by counting the cold neutrons reaching the detector, while the proton beam is redirected to ISIS TS2. Transmission measurements were acquired using the ^{6}Li-doped glass scintillator equipped on the VESUVIO beamline, whose position calibration and background characterization have been discussed in Ref. 30.

E. Monte Carlo simulations

Monte Carlo (MC) transport simulations were performed to assess the impact on radiation protection of a more accurate air cross section model. The Geant4 toolkit (version 11.3.2),[33] integrated with the NCrystal toolkit[34] was exploited, providing a computational environment, compatible with multiple MC packages, facilitating the implementation of new cross section libraries into transport simulations. To simulate neutron transport in the nuclear gas approximation, we employed the reference physics list QGSP_BIC_HP, available within the Geant4 toolkit. This physics list, often employed in medical physics applications, is one of the few Geant4 reference physics lists that account for neutrons with energies below 20 MeV, which is, therefore, marked as "high precision" (HP).[35] The neutron transport simulations in the molecular gas approximation are implemented with the use of the NCrystal toolkit, in conjunction with the QGSP_BIC_HP physics list. In fact, NCrystal overrides Geant4's default scattering cross section for neutrons in the thermal energy range. In both cases, we simulated the transport of monochromatic thermal neutrons (10, 25, and 50 meV) in a 3 × 3 × 3 m^3 cube, as shown in Fig. 1, filled with dry air of density 0.001 225 g/cm^3 at a reference temperature of 293.6 K. The neutron beam strikes the center of one face of the cube at Z = −1.5 m, traveling along the positive Z-axis. The beam has a cross-sectional area of 5 × 5 cm^2, and its divergence is neglected. Scoring was implemented through a custom sensitive detector and hit classes, which recorded the energy and position coordinates of neutrons at the boundary with the air filled room. A transmission detector was also added directly next to the box, right in front of the beam trajectory, for comparison with expected transmission values. The agreement between the Geant4-simulated transmission spectrum and the molecular gas model used to simulate it (see Fig. 10) confirms that the contribution of scattered neutrons to transmission is negligible.

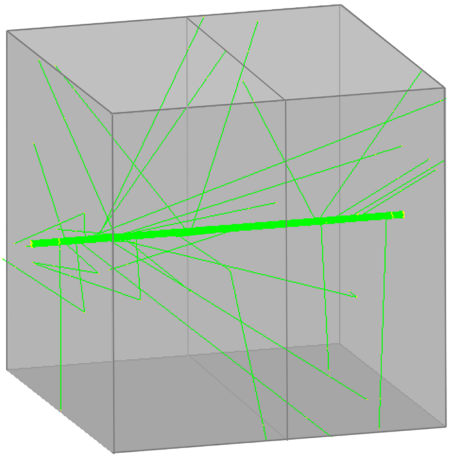

FIG. 1. Schematics of the used geometry for Monte Carlo simulations. The room is of dimensions 3 × 3× 3 m^3. The incident neutron beam direction, corresponding to the thick green line, is oriented along the *z* axis. The origin of the axes is placed at the center of the box. Thinner green lines correspond to scattered neutron trajectories.

F. Free nuclear gas model

The neutron scattering from room-temperature gases is often approximated as the scattering from a gas of free nuclei, with an energy-dependent scattering cross section,

$$\sigma_s(\xi) = \frac{\sigma_b}{\left(1+\frac{1}{M}\right)^2}\left[\left(1+\frac{1}{2\xi^2}\right)\mathrm{erf}(\xi) + \frac{e^{-\xi^2}}{\sqrt{\pi}\xi}\right], \tag{16}$$

having defined $\xi^2 = ME/k_BT$. This equation represents the default estimate of the scattering cross section by thermal neutrons in most Monte Carlo codes, assuming that all matter is composed of free nuclei. In some cases, e.g., for molecular systems, the nuclear mass M can be replaced with an effective mass, M_e, partially taking into consideration the rotations of the molecule according to the Sachs and Teller formalism.[13] In Ref. 2, the authors used $M_e = 9$ for N in N_2 and $M_e = 10$ for O in O_2, although the effective Sachs–Teller mass for diatomic molecules is $M_e = 1.2M$ (see, for example, Ref. 36. Equation (16) can provide a better approximation of experimental data when an effective temperature is used, which takes into consideration the actual nuclear kinetic energy of each nucleus due to translational, rotational, and vibrational modes.[37,38]

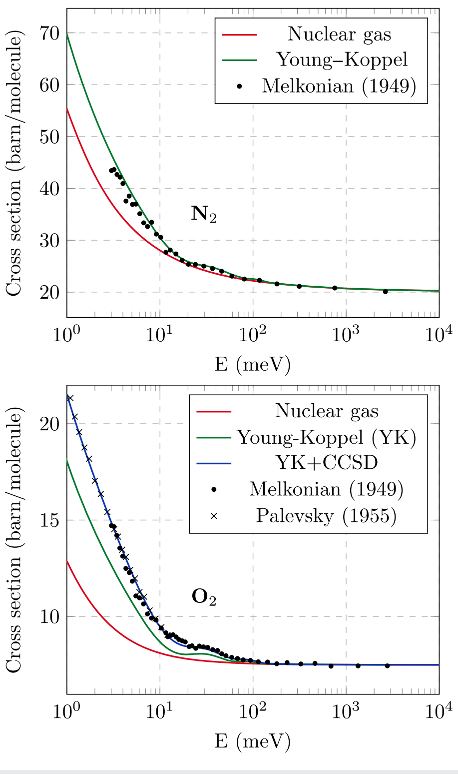

FIG. 2. Total cross sections of N_2 (top panel) and O_2 (bottom panel). Free nuclear gas models are reported as red lines, using the actual mass. The result using a YK model to account for nuclear scattering from rotational states is reported as a green solid line. In the case of O_2, the total cross section, including magnetic scattering from molecular-orbital electrons, is reported as a blue line. Experimental data are from Ref. 3 (circle markers) and Ref. 39 (cross markers).

III. RESULTS AND DISCUSSION

Figure 2 shows the total cross section of N_2 (top) and O_2 (bottom) obtained by calculating the scattering contribution using Eq. (16) and the actual nuclear mass (red solid lines). In both cases, experimental data from Ref. 3 down to 3 meV are also reported, as well as data from Ref. 39 in the case of molecular oxygen. One can easily appreciate that a free nuclear gas approach [Eq. (16)] is most suitable at epithermal energies, already at hundreds of meV, for both molecules. At these energies, neutron scattering is not significantly affected by quantized transitions between rotational states (expected at tens of meV).

While the simple model in Eq. (16) provides a satisfactory description of the epithermal part of the cross section, it significantly underestimates the thermal part. By considering free nuclei, one neglects all possible transitions between rotational states. As mentioned, tens of initial and final states need to be considered in the Fermi golden rule to reach the convergence of the double differential cross section. This also reflects on the total cross section in a nontrivial dependence upon the neutron energy in the region between 10 and 100 meV, which completely escapes a simplified model of

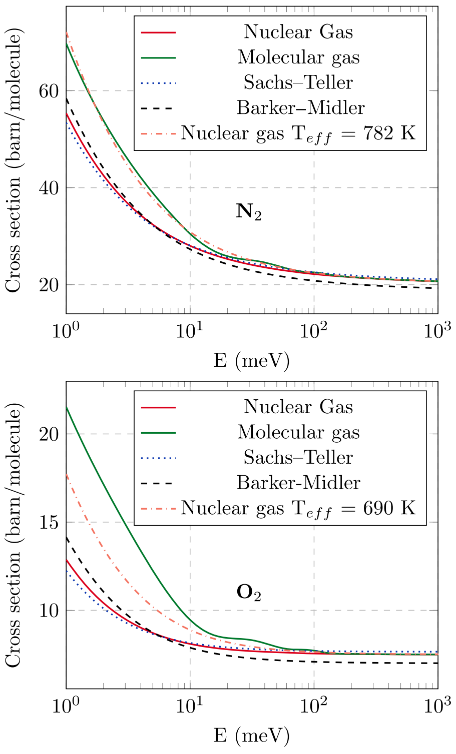

FIG. 3. Total cross section models of N_2 (top panel) and O_2 (bottom panel) for comparison. Free nuclear gas models are reported as red solid lines, while Sachs–Teller models are represented by the black dashed lines (effective masses by Barker–Midler) and blue dotted lines (canonical effective mass $M_e = 1.2M$). Molecular gas models (YK for N_2 and YK + CCSD for O_2) are reported as green solid lines. The orange dashed lines represent the use of the model for the free nuclear gas with effective temperatures, as discussed in the text.

scattering from structureless nuclei. In the case of molecular nitrogen, which is the most abundant molecular species in atmospheric air, one can appreciate how a suitable description of the total cross section can only be achieved through a treatment of the molecule using the YK model. The calculation, reported as a green line in the top panel of Fig. 2, satisfactorily overlaps with the experimental data without any need for effective or fitting parameters.

The attempt, within the Sachs–Teller approximation, to effectively account for the rotational dynamics of the molecule through a revised value of the nuclear mass, is represented by the dashed curves in Fig. 3 for both N_2 (top) and O_2 (bottom). By using the effective mass discussed in Barker–Midler,[2] one slightly increases the thermal scattering at incident neutron energies lower than about 40 meV, yet spoils the comparison at epithermal energies. A better approximation of the experimental data is obtained by using Eq. (16) with an effective temperature, taking into consideration the nuclear motion of each nucleus due to translational, rotational, and vibrational motions. The result of this approximation is reported in Fig. 3 as an orange dashed line, considering effective temperatures of 782 and 690 K for nitrogen and oxygen, respectively.

In the case of molecular oxygen, while the YK model already provides a result much improved compared to a free nuclear gas, the comparison with the experimental data is still not satisfactory, as one can appreciate from the bottom panel of Fig. 2. As mentioned, and as is well known, low-energy thermal neutrons can interact with the unpaired electrons of the outer molecular orbital of O_2, which is responsible for the molecule's paramagnetism. Figure 4 reports the radial electron spin density as calculated using first-principles approaches and an *ab initio* MD simulation. These calculations represent the state of the art in computer modeling of molecular systems and allow us to overcome the approximations and uncertainties of previous treatments of magnetic scattering from O_2. An initial inspection of Fig. 4 shows how the spatial spin density cannot be surmised from effective atomic orbitals related to hydrogen-like solutions of the Schrödinger equation. The dashed line in the figure shows how such an approximation would localize the spin density to shorter distances compared to molecular orbitals. Moreover, a more detailed inspection of the figure shows how the calculations based on DFT or CCSD and MD yield approximately overlapping results, with a small difference observed between 2 and 5 Å with respect to the molecule center of mass.

The results shown in Fig. 4 were used to calculate the magnetic scattering for O_2, as shown in Fig. 5. The calculation based on DFT or CCSD and *ab initio* MD provide overlapping values for the magnetic scattering, which are in good agreement with the experimental values from Ref. 39. Meanwhile, theoretical predictions from Ref. 10 below 1 meV feature a nonphysical increase at low energies, in contrast to the expected limiting value of the magnetic cross section, related to the limit $f(Q) \to 1$ as $Q \to 0$. This condition, reported as a dashed horizontal line in Fig. 5, is correctly satisfied by our calculations. By considering this additional magnetic scattering contribution to the total cross section, one obtains the blue solid line in the bottom panel of Fig. 2, which satisfactorily overlaps with the experimental data from the literature.

It is worth noting an apparent discrepancy between the magnetic scattering formulations in Refs. 12 and 10, related to the intensity correction from the Debye–Waller factor $W(Q)$. Such a factor is proportional to the mean square displacement of nuclei within a molecular system or a crystal. Having in mind the uncertainty principle, higher displacements are expected in the case of

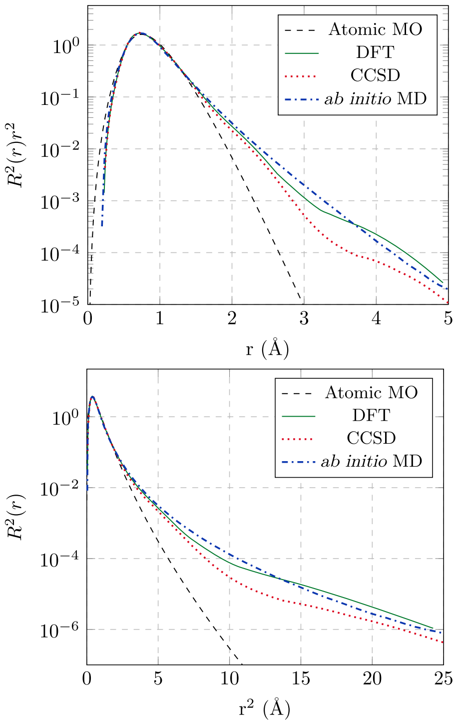

FIG. 4. Square of the radial spin density, $R(r)$, of electron in the O_2 external molecular orbital (bottom panel), also including multiplication by the square of the distance from the molecule center of mass r (top panel), for a hydrogen-like atomic orbital (black dashed line), CCSD/aug-cc-pVTZ (red dotted line), DFT - B3LYP/aug-cc-pVTZ (green solid line), and from *ab initio* MD simulations (dotted-dashed blue line).

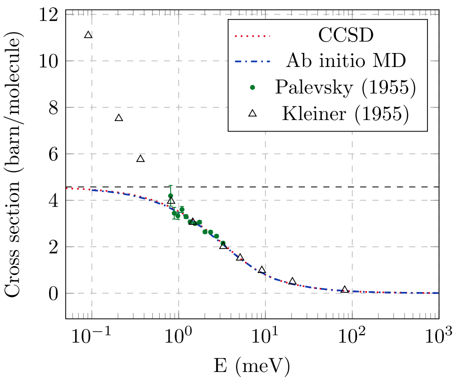

FIG. 5. Magnetic scattering cross section from O_2 as calculated from CCSD (red dotted line) and *ab initio* MD (blue dashed line), as compared with the experimental data from Ref. 39 (green dot markers) and theoretical data from Ref. 10 (empty triangle markers). The black dashed line represents the limiting value for $f(Q) \simeq 1$ for low neutron energies. Please note that the results from CCSD and *ab initio* MD practically overlap.

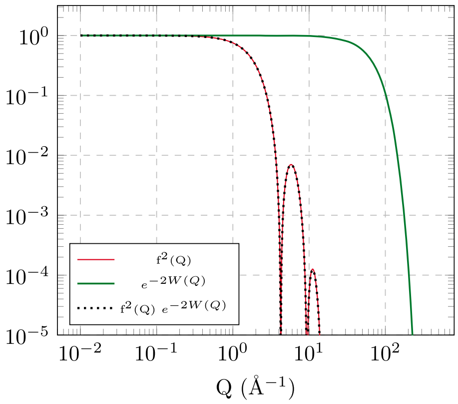

FIG. 6. Magnetic form factor $f^2(Q)$ (red) and the Debye–Waller factor correction (green) as a function of the scattering vector **Q**. Their product is reported as a black dotted line.

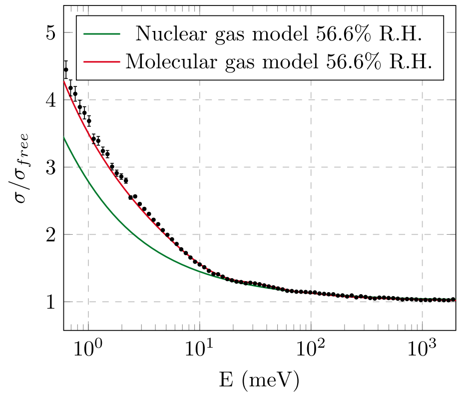

FIG. 7. Experimental measurement of the total cross section of air (black error bars) at a monitored temperature (293.6 K), 1 bar, and relative humidity (56.5%), as compared with a nuclear gas model (green) and a molecular gas model (red).

lower-energy vibrational modes, such as phonons in a crystal, while lower values of the total nuclear mean-square displacement are expected in the case of a small molecule, featuring only a high-energy vibrational stretching mode. For this reason, the deviation from the unity of the Debye–Waller factor only happens, in the case of O_2, in a Q range, where the magnetic form factor has already reached negligible intensities, and one can approximate the product of the two terms in Eq. (14) as

$$e^{-2W(Q)} f^2(Q) \simeq f^2(Q), \tag{17}$$

as one can visually appreciate from Fig. 6.

Having modeled the two most abundant molecular components of air, we used our calculation to compose a total scattering cross section of air at a given humidity level. Figure 7 provides the comparison of our model (red line) with the experimental data measured on VESUVIO at 294.9 K and 56.5% relative humidity (black error bars). The comparison, reported in this figure only for thermal neutrons, is considered satisfactory in the neutron energy range between 0.6 meV and 10 keV. The model includes N_2 and O_2 described by YK models and magnetic scattering, a water contribution based on the thermal cross section of the liquid at room temperature,[40] and Ar approximated with a free nuclear gas model. One should note the larger error bars in our results for energies between 0.6 and 3 meV. This is linked to the procedure to acquire ToF transmission spectra on the instrument, in the so-called extended energy range described in Ref. 32. Data are reported as normalized to the epithermal scattering cross section, obtained as the weighted sum of the free scattering cross section of all elements in the system. This procedure provides a way to report on the thermal cross section independently of the thickness of the sample, which is otherwise a source of systematic errors. However, one should notice that solid knowledge of the free scattering cross section of the elements under investigation is required, as well as the (more unique) possibility to perform measurements at thermal and epithermal neutron energies at the same time, with no need to modify the acquisition setup. This is a key ability of VESUVIO, able to access an energy range summing up to 8 orders of magnitude within the same measurement.

The comparison with the cross section from a free nuclear gas model is reported as a green line in Fig. 7. Similarly to what has been discussed in the case of N_2 and O_2, deviations from a free nuclear gas model become increasingly important at lower neutron energies. At 1 meV, the difference between the two models is about 25%. Differences between the simplified modeling and the experimental data are of the same order of magnitude as those reported in Ref. 2 and can be readily related to the neglect of the molecular contributions to the total cross section. By the inspection of Fig. 8, one can see how the inclusion of molecular contributions in dry air (solid and dashed lines for molecular and nuclear gases, respectively) is much more important than the inclusion of water vapor (red and blue lines for dry and 56.5% R.H., respectively). It is undeniable that the modeling of such molecular contributions in nuclear-oriented Monte Carlo transport codes can be challenging. However, through the use of modules, such as the NCrystal module for Geant4, one can load pre-calculated scattering libraries. Below, we provide a discussed example.

Figure 9 shows the results of an MC simulation within the environmental box described in Fig. 1, making use of free nuclear

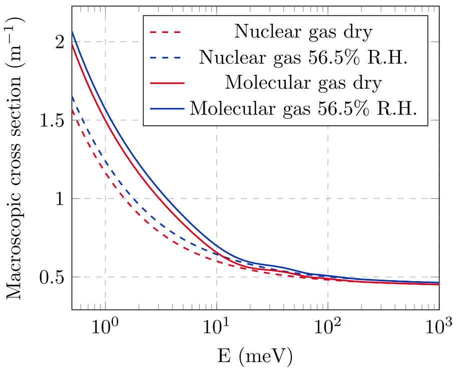

FIG. 8. Macroscopic cross section as calculated from a free nuclear gas model (dashed) and a molecular gas model (solid) for a dry air mixture (red), with a relative humidity of 56.5% (blue).

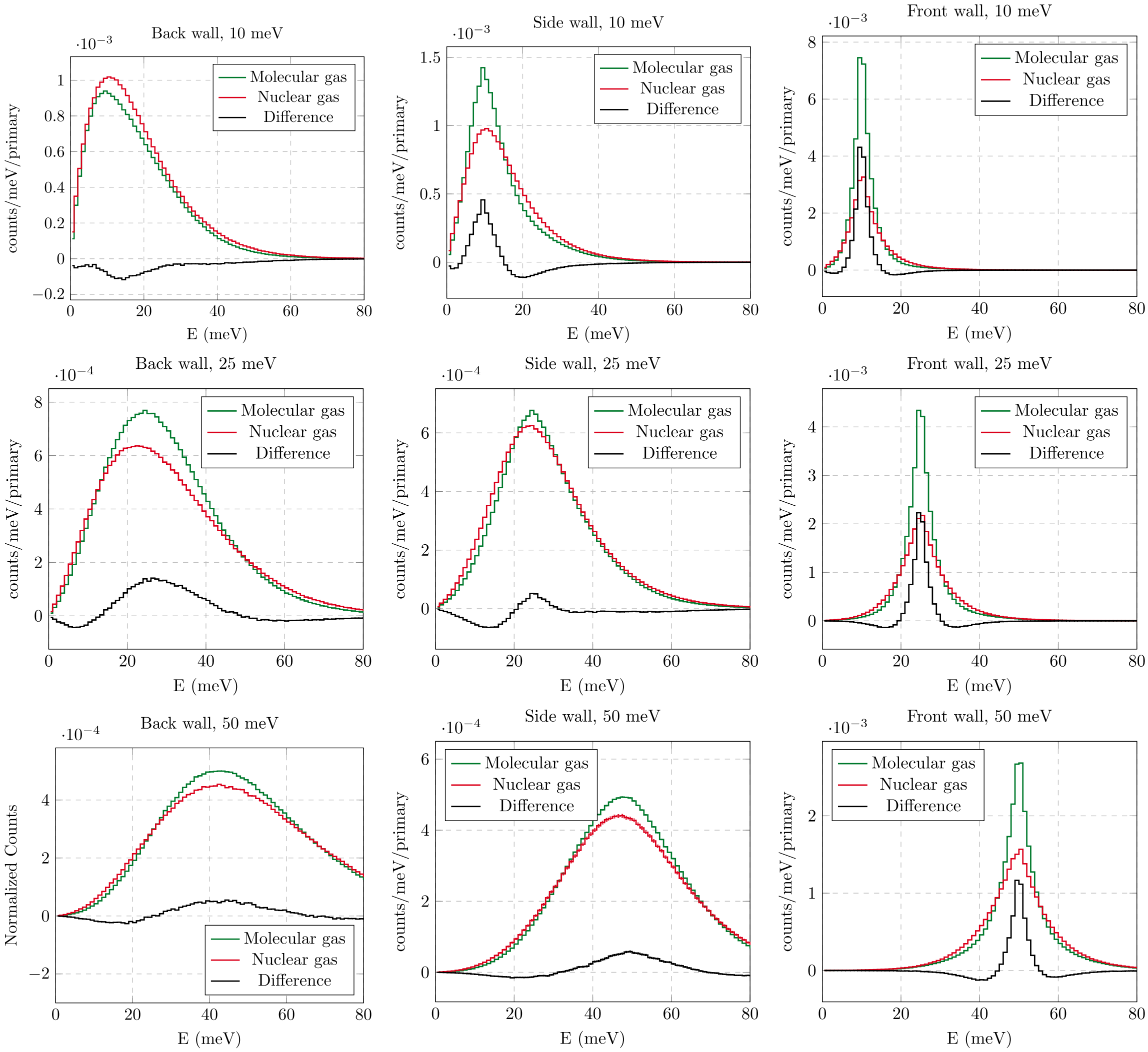

FIG. 9. Neutron counts on the walls of a 3 × 3 × 3 m^3 room in the case of neutron energy beams of 10, 25, and 50 meV (top, middle, and bottom rows). Results using molecular and nuclear gas models are reported as green and red lines, respectively, while the difference between the two cases is reported as black lines. Results are reported separately for the back, side, and front walls, corresponding to the left, center, and right columns.

gas (red lines) and molecular gas (green lines) thermal cross sections. The results are provided for back, side, and front walls in the environment box, as defined based on the propagation direction of primary neutrons. Simulations are provided for three energies, at 10, 25, and 50 meV (first, second, and third rows, respectively), and counts are normalized to the number of primary neutrons simulated (10^8). Absolute differences are reported as black lines. In all cases, one can observe both a higher number of scattered neutrons when molecular models are used and a different distribution of final neutron energies. From the directionality of the scattered neutrons, one can see how forward scattering is more likely in the case of molecular modeling. Backward and sideward scattered neutrons feature shifts in their energy distributions between the two models. In the case of forward scattering, the distribution of scattered neutrons is more centered around the elastic line, with a sharp signature at the same energy as the initial energy, which can also be observed with a lower intensity in the panels related to sideward-scattered neutrons.

One should notice that, depending on the energy and direction of scattered neutrons, the relative differences in Fig. 9 can be as large as 20%–30%. Such an effect, related to the up-scattering and down-scattering interactions of neutrons with rotational states, is expected to play a role in the activation and radiation protection of a laboratory or medical facility featuring neutrons traveling in air rather than in vacuum tubes, specifically in relation to the reactions reported in Table II. The redistribution to higher energies, observed with our modeling, could be a welcome result within the framework of

TABLE II. List of neutron absorption processes included in the Monte Carlo simulation.

Isotope	Mol. % in dry air	Mol. % in hydrated air	Reaction	$\sigma_a(E_0)$ (barn)
^{14}N	0.7848	0.7696	$^{14}N(n,\gamma)^{15}N$ $^{14}N(n,p)^{14}C$	0.075 1.84
^{16}O	0.2105	0.2064 in O_2 0.0065 in H_2O	$^{16}O(n,\gamma)^{17}O$	0.0001
^{40}Ar	0.0047	0.0046	$^{40}Ar(n,\gamma)^{41}Ar$	0.66
^{1}H	0	0.0129	$^{1}H(n,\gamma)^{2}H$	0.3326

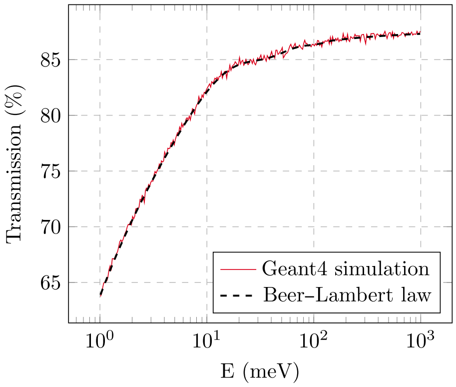

FIG. 10. The Geant4-simulated transmission spectrum (red solid line) is compared to the molecular gas model of dry air (black dashed line) used in the simulation. The observed agreement confirms the validity of the "good geometry" approximation.

radiation protection, considering that many neutron-induced activations are inversely proportional to the neutron velocity. At the same time, the higher number of neutrons scattered in the forward direction should be carefully considered when planning a shielding wall in a medical facility, as well as when large-surface detectors are used on a research facility.

Finally, Fig. 10 provides an *a posteriori* test of the validity of the good-geometry approximation within our experimental setup. This figure shows the analytical application of the Beer–Lambert law using the cross section of air developed in this work, compared to the result of the Monte Carlo simulation of our transmission experiment, which takes into account neutrons scattered within the extended sample volume and the surrounding gas and then redirected toward and detected by the transmission monitor. The complete overlap of the two calculations shows that the contribution of such scattered neutrons is negligible compared to the number of purely transmitted neutrons.

IV. CONCLUSION

Modeling of the thermal neutron cross section of O_2 and N_2 based on *ab initio* state-of-the-art molecular simulations, which include a detailed evaluation of magnetic contributions, has allowed us to provide a more accurate description of the thermal neutron cross section of air. Moreover, we have provided new experimental data regarding the total cross section of air, under controlled thermophysical conditions, showing that only a proper inclusion of molecular contributions to the neutron cross section allows a satisfactory modeling of experimental data. In addition, we have quantified the underestimate of free nuclear gas cross sections to about 25% at 1 meV, and we have shown how the inclusion of water vapor is a second-order effect compared to molecular contributions.

Finally, we have provided Monte Carlo simulations, where we make use of our modeling in the form of a revised material definition within the NCrystal module in Geant4. In the case of thermal neutron transport in a room, with dimensions similar to sample-environment neutron beamlines or medical facilities, we have shown how the inclusion of molecular contributions brings an increase in scattered neutrons as well as a redistribution of their energies, with respect to a traditional simulation making use of free nuclear gas cross sections.

ACKNOWLEDGMENTS

The authors acknowledge the financial support from the Consiglio Nazionale delle Ricerche under the CNR-STFC Grant Agreement No. 2021–2027 concerning collaboration in scientific research at the ISIS (UK) of STFC. The STFC Rutherford Appleton Laboratory is acknowledged for access to neutron beam facilities. Support from the IKUR Strategy under the collaboration agreement between the Ikerbasque Foundation and the Materials Physics Center, on behalf of the Department of Science, Universities & Innovation of the Basque Government, is acknowledged.

AUTHOR DECLARATIONS

Conflict of Interest

The authors have no conflicts to disclose.

Author Contributions

Margherita Simoni: Data curation (equal); Formal analysis (equal); Investigation (equal); Methodology (equal); Software (equal); Validation (equal); Writing – original draft (equal). **Felix Fernandez-Alonso**: Conceptualization (equal); Methodology (equal); Writing – review & editing (equal). **Tommaso Giovannini**: Methodology (equal); Software (equal); Writing – review & editing (equal).

Matthew Krzystyniak: Investigation (equal); Methodology (equal); Writing – review & editing (equal). **Jose Ignacio Marquez Damian**: Methodology (equal); Software (equal); Writing – review & editing (equal). **Anna Marsicano**: Investigation (equal); Methodology (equal); Writing – review & editing (equal). **Marco Martellucci**: Methodology (equal); Writing – review & editing (equal). **Triestino Minniti**: Methodology (equal); Software (equal); Writing – review & editing (equal). **Roberto Senesi**: Conceptualization (equal); Funding acquisition (equal); Methodology (equal); Writing – original draft (equal). **Matteo Sorbara**: Methodology (equal); Software (equal); Writing – review & editing (equal). **Giovanni Romanelli**: Conceptualization (equal); Investigation (equal); Methodology (equal); Project administration (equal); Software (equal); Supervision (equal); Validation (equal); Writing – original draft (equal).

DATA AVAILABILITY

The data that support the findings of this article are openly available at https://doi.org/10.5286/ISIS.E.RB2410241-1.[31] Modeling of the thermal scattering of O_2 and N_2 was obtained through the Python script at https://colab.research.google.com/drive/16vNFLXhfcomOcZ5xsb8l2qt9-zrQd0zW?usp=sharing.

REFERENCES

[1] S. J. Seestrom, E. R. Adamek, D. Barlow, L. J. Broussard, N. B. Callahan, S. M. Clayton, C. Cude-Woods, S. Currie, E. B. Dees, W. Fox, P. Geltenbort, K. P. Hickerson, A. T. Holley, C.-Y. Liu, M. Makela, J. Medina, D. J. Morley, C. L. Morris, J. Ramsey, A. Roberts, D. J. Salvat, A. Saunders, E. I. Sharapov, S. K. L. Sjue, B. A. Slaughter, B. VornDick, P. L. Walstrom, Z. Wang, T. L. Womack, A. R. Young, and B. A. Zeck (UCNτ Collaboration), "Upscattering of ultracold neutrons from gases," Phys. Rev. C **92**, 065501 (2015).

[2] J. G. Barker and D. F. R. Mildner, "Survey of background scattering from materials found in small-angle neutron scattering," J. Appl. Crystallogr. **48**, 1055–1071 (2015).

[3] E. Melkonian, "Slow neutron velocity spectrometer studies of O_2, N_2, A, H_2, H_2O, and seven hydrocarbons," Phys. Rev. **76**, 1750–1759 (1949).

[4] F. Atchison, B. van den Brandt, T. Bryś, M. Daum, P. Fierlinger, P. Hautle, R. Henneck, K. Kirch, J. Kohlbrecher, G. Kühne, J. A. Konter, A. Pichlmaier, A. Wokaun, K. Bodek, M. Kasprzak, M. Kuźniak, P. Geltenbort, M. Giersch, J. Zmeskal, M. Hino, and M. Utsuro, "Measured total cross sections of slow neutrons scattered by gaseous and liquid $^2H_2$," Phys. Rev. Lett. **94**, 212502 (2005).

[5] G. Bison, R. Grössle, K. Kirch, B. Lauss, F. Priester, I. Rienäcker, and G. Zsigmond, "Temperature-dependent ultracold neutron transmission in $^2H_2$ gas: A test of the Young-Koppel model," Phys. Rev. C **112**, 014007 (2025).

[6] V. F. Sears, "Neutron scattering lengths and cross sections," Neutron News **3**, 26–37 (1992).

[7] K. B. Grammer *et al.*, "Measurement of the scattering cross section of slow neutrons on liquid parahydrogen from neutron transmission," Phys. Rev. B **91**, 180301 (2015).

[8] J. A. Young and J. U. Koppel, "Slow neutron scattering by molecular hydrogen and deuterium," Phys. Rev. **135**, A603–A611 (1964).

[9] O. Halpern and G. L. Appleton, "The scattering of slow neutrons by O_2 molecules," Phys. Rev. **90**, 869–879 (1953).

[10] W. H. Kleiner, "Magnetic scattering of slow neutrons from O_2 gas," Phys. Rev. **97**, 411–418 (1955).

[11] S. Mühlbauer, D. Honecker, É. A. Périgo, F. Bergner, S. Disch, A. Heinemann, S. Erokhin, D. Berkov, C. Leighton, M. R. Eskildsen, and A. Michels, "Magnetic small-angle neutron scattering," Rev. Mod. Phys. **91**, 015004 (2019).

[12] A. T. Boothroyd, *Principles of Neutron Scattering from Condensed Matter* (Oxford University Press, 2020).

[13] R. G. Sachs and E. Teller, "The scattering of slow neutrons by molecular gases," Phys. Rev. **60**, 18–27 (1941).

[14] M. Hollas, *Modern Spectroscopy* (John Wiley & Sons, 2005), Vol. 82.

[15] S. W. Lovesey and J. W. Lynn, *Theory of Neutron Scattering from Condensed Matter* (Oxford University Press, 1986), Vol. 1 and 2.

[16] W. Langel, D. L. Price, R. O. Simmons, and P. E. Sokol, "Inelastic neutron scattering from liquid and solid hydrogen at high momentum transfer," Phys. Rev. B **38**, 11275–11283 (1988).

[17] C. Stassis and H. W. Deckman, "Magnetic scattering of neutrons," Phys. Rev. B **12**, 1885 (1975).

[18] J. H. Van Vleck, *The Theory of Electric and Magnetic Susceptibilities*, *International Series of Monographs on Physics* (The Clarendon Press, Oxford, 1932).

[19] T. Helgaker, P. Jorgensen, and J. Olsen, *Molecular Electronic-Structure Theory* (John Wiley & Sons, 2014).

[20] A. D. Becke, "Density-functional thermochemistry. III. The role of exact exchange," J. Chem. Phys. **98**, 5648–5652 (1993).

[21] P. J. Stephens, F. J. Devlin, C. F. Chabalowski, and M. J. Frisch, "Ab initio calculation of vibrational absorption and circular dichroism spectra using density functional force fields," J. Phys. Chem. **98**, 11623–11627 (1994).

[22] F. Neese, "Software update: The orca program system—version 5.0," Wiley Interdiscip. Rev.: Comput. Mol. Sci. **12**, e1606 (2022).

[23] S. J. Clark, M. D. Segall, C. J. Pickard, P. J. Hasnip, M. I. J. Probert, K. Refson, and M. C. Payne, "First principles methods using castep," Z. fur Krist. - Cryst. Mater. **220**, 567–570 (2005).

[24] A. Picard, R. S. Davis, M. Gläser, and K. Fujii, "Revised formula for the density of moist air (CIPM-2007)," Metrologia **45**, 149 (2008).

[25] Ncrystal – H_2O-Online, available online at https://raw.githubusercontent.com/wiki/mctools/ncrystal/datalib/LiquidWaterHosub42o/sub4O_T293.6K.nc.

[26] J. I. Màrquez-Damiàn, J. R. Granada, and D. C. Malaspina, "CAB models for water: A new evaluation of the thermal neutron scattering laws for light and heavy water in ENDF-6 format," Ann. Nucl. Energy **65**, 280–289 (2014).

[27] J. I. M. Damian, D. C. Malaspina, and J. R. Granada, "Vibrational spectra of light and heavy water with application to neutron cross section calculations," J. Chem. Phys. **139**, 024504 (2013).

[28] K. Yoshida, C. Wakai, N. Matubayasi, and M. Nakahara, "A new high-temperature multinuclear-magnetic-resonance probe and the self-diffusion of light and heavy water in sub- and supercritical conditions," J. Chem. Phys. **123**, 164506 (2005).

[29] R. Mills, "Self-diffusion in normal and heavy water in the range 1-45 deg," J. Phys. Chem. **77**, 685–688 (1973).

[30] J. I. Robledo, J. Dawidowski, J. I. M. Damián, G. Škoro, C. Bovo, and G. Romanelli, "Measurement of neutron total cross sections at the VESUVIO spectrometer," Nucl. Instrum. Methods Phys. Res., Sect. A **971**, 164096 (2020).

[31] G. Romanelli, T. Minniti, M. Simoni, C. Cazzaniga, C. Andreani, A. Russo, M. Krzystyniak, and R. Senesi, "Validation of new thermal scattering libraries for the moderation of epithermal neutrons in phantom materials," 2024, https://doi.org/10.5286/ISIS.E.RB2410241-1, ISIS Experiment No: RB2410241.

[32] G. Romanelli, M. Krzystyniak, R. Senesi, D. Raspino, J. Boxall, D. Pooley, S. Moorby, E. Schooneveld, N. J. Rhodes, C. Andreani, and F. Fernandez-Alonso, "Characterisation of the incident beam and current diffraction capabilities on the VESUVIO spectrometer," Meas. Sci. Technol. **28**, 095501 (2017).

[33] S. Agostinelli, J. Allison, K. Amako, J. Apostolakis, H. Araujo, P. Arce, M. Asai, D. Axen, S. Banerjee, G. Barrand, F. Behner, L. Bellagamba, J. Boudreau, L. Broglia, A. Brunengo, H. Burkhardt, S. Chauvie, J. Chuma, R. Chytracek, G. Cooperman, G. Cosmo, P. Degtyarenko, A. Dell'Acqua, G. Depaola, D. Dietrich, R. Enami, A. Feliciello, C. Ferguson, H. Fesefeldt, G. Folger, F. Foppiano, A. Forti, S. Garelli, S. Giani, R. Giannitrapani, D. Gibin, J. J. Gómez Cadenas, I. González, G. Gracia Abril, G. Greeniaus, W. Greiner, V. Grichine, A. Grossheim, S. Guatelli, P. Gumplinger, R. Hamatsu, K. Hashimoto, H. Hasui, A. Heikkinen, A. Howard, V. Ivanchenko, A. Johnson, F. W. Jones, J. Kallenbach, N. Kanaya, M. Kawabata, Y. Kawabata, M. Kawaguti, S. Kelner, P. Kent, A. Kimura, T. Kodama, R. Kokoulin, M. Kossov, H. Kurashige, E. Lamanna, T. Lampén, V. Lara, V. Lefebure, F. Lei, M. Liendl, W. Lockman, F. Longo, S. Magni, M. Maire, E. Medernach, K. Minamimoto, P. Mora de Freitas, Y. Morita, K. Murakami, M. Nagamatu, R. Nartallo, P. Nieminen, T. Nishimura, K. Ohtsubo, M. Okamura, S. O'Neale, Y. Oohata, K. Paech, J. Perl, A. Pfeiffer, M. G. Pia, F. Ranjard, A. Rybin, S. Sadilov, E. Di Salvo,

G. Santin, T. Sasaki, N. Savvas, Y. Sawada, S. Scherer, S. Sei, V. Sirotenko, D. Smith, N. Starkov, H. Stoecker, J. Sulkimo, M. Takahata, S. Tanaka, E. Tcherniaev, E. Safai Tehrani, M. Tropeano, P. Truscott, H. Uno, L. Urban, P. Urban, M. Verderi, A. Walkden, W. Wander, H. Weber, J. P. Wellisch, T. Wenaus, D. C. Williams, D. Wright, T. Yamada, H. Yoshida, and D. Zschiesche, "Geant4—a simulation toolkit," Nucl. Instrum. Methods Phys. Res., Sect. A **506**, 250–303 (2003).

[34] X.-X. Cai and T. Kittelmann, "Ncrystal: A library for thermal neutron transport," Comput. Phys. Commun. **246**, 106851 (2020).

[35] J. Allison, K. Amako, J. Apostolakis, P. Arce, M. Asai, T. Aso, E. Bagli, A. Bagulya, S. Banerjee, G. Barrand, B. R. Beck, A. G. Bogdanov, D. Brandt, J. M. C. Brown, H. Burkhardt, P. Canal, D. Cano-Ott, S. Chauvie, K. Cho, G. A. P. Cirrone, G. Cooperman, M. A. Cortés-Giraldo, G. Cosmo, G. Cuttone, G. Depaola, L. Desorgher, X. Dong, A. Dotti, V. D. Elvira, G. Folger, Z. Francis, A. Galoyan, L. Garnier, M. Gayer, K. L. Genser, V. M. Grichine, S. Guatelli, P. Guèye, P. Gumplinger, A. S. Howard, I. Hřivnáčová, S. Hwang, S. Incerti, A. Ivanchenko, V. N. Ivanchenko, F. W. Jones, S. Y. Jun, P. Kaitaniemi, N. Karakatsanis, M. Karamitros, M. Kelsey, A. Kimura, T. Koi, H. Kurashige, A. Lechner, S. B. Lee, F. Longo, M. Maire, D. Mancusi, A. Mantero, E. Mendoza, B. Morgan, K. Murakami, T. Nikitina, L. Pandola, P. Paprocki, J. Perl, I. Petrović, M. G. Pia, W. Pokorski, J. M. Quesada, M. Raine, M. A. Reis, A. Ribon, A. Ristić Fira, F. Romano, G. Russo, G. Santin, T. Sasaki, D. Sawkey, J. I. Shin, I. I. Strakovsky, A. Taborda, S. Tanaka, B. Tomé, T. Toshito, H. N. Tran, P. R. Truscott, L. Urban, V. Uzhinsky, J. M. Verbeke, M. Verderi, B. L. Wendt, H. Wenzel, D. H. Wright, D. M. Wright, T. Yamashita, J. Yarba, and H. Yoshida, "Recent developments in GEANT4," Nucl. Instrum. Methods Phys. Res., Sect. A **835**, 186–225 (2016).

[36] M. G. Izzo, F. Bencivenga, A. Cunsolo, S. Di Fonzo, R. Verbeni, and R. G. De Lorenzo, "The single particle dynamics of iodine in the Sachs–Teller regime: An inelastic x-ray scattering study," J. Chem. Phys. **133**, 124514 (2010).

[37] C. Andreani, M. Krzystyniak, G. Romanelli, R. Senesi, and F. Fernandez-Alonso, "Electron-volt neutron spectroscopy: Beyond fundamental systems," Adv. Phys. **66**, 1–73 (2017).

[38] M. Nelkin, "Scattering of slow neutrons by water," Phys. Rev. **119**, 741 (1960).

[39] H. Palevsky and R. M. Eisberg, "Magnetic scattering of slow neutrons by gaseous oxygen," Phys. Rev. **98**, 492 (1955).

[40] J. I. M. Damián, J. R. Granada, and D. C. Malaspina, "New thermal neutron scattering kernels for light and heavy water based on molecular dynamics simulations," Phys. Procedia **60**, 300–309 (2014).